Journal of Materials Research and Technology 31 (2024) 3591–3603

Contents lists available at ScienceDirect

Journal of Materials Research and Technology

journal homepage: www.elsevier.com/locate/jmrt

Design of Ni-rGO reinforced Sn2.5Ag0.7Cu0.1Ce composite solder based on micro-alloying and composite principles: Microstructure and properties

Fupeng Huo [a], Chuantong Chen [a,*], Zheng Zhang [a], Yicheng Zhang [a], Aiji Suetake [a], Kazutaka Takeshita [c], Yoshiji Yamaguchi [c], Yashima Momose [c], Keke Zhang [b,**], Katsuaki Suganuma [a]

[a] Flexible 3D System Integration Laboratory, The Institute of Science and Industrial Research, Osaka University, Osaka, 565-0871, Japan
[b] School of Materials Science and Engineering, Henan University of Science and Technology, Luoyang, 471023, China
[c] Yamato Scientific Co. Ltd., Tokyo, 104-0053, Japan

ARTICLE INFO

Handling editor: SN Monteiro

Keywords:
SnAgCu
Graphene
Microstructure
Surface metallization
Mechanical properties
Wettability

ABSTRACT

Based on the principles of micro-alloying and composite, the graphene reinforced Sn2.5Ag0.7Cu0.1Ce composite solder was designed. Ni nanoparticle-modified reduced graphene oxide (Ni-rGO) was prepared by thermal decomposition method, and the powder-melting method was proposed for the first time to prepare Ni-rGO reinforced Sn2.5Ag0.7Cu0.1Ce composite solder. The microstructure, wettability, electrical resistivity, and mechanical properties of the composite solder were systematically studied. Results indicated that the Ni nanoparticles uniformly adhered to the rGO with a size of 26.3 nm. The effective incorporation of Ni-rGO into the solder matrix was achieved. The result broke the technical difficulty that graphene cannot be effectively added to low melting point metals. With the addition of Ni-rGO, the grain size gradually decreased, and the eutectic structures increased. Deep etching results revealed that columnar β-Sn was stacked from layered β-Sn, the addition of 0.05 wt% Ni-rGO led to an increase in sheet-like Ag_3Sn within the eutectics. Additionally, Ni-rGO was found at the grain boundaries of composite solder, serving as nucleation sites for Ag_3Sn and Cu_6Sn_5. At an addition of 0.05 wt%, the tensile strength reaches a maximum of 58.1 MPa, with elongation of 33.8%, surpassing the strength of commercial Sn3.0Ag0.5Cu solder. Therefore, the high-strength and tough composite solder was obtained. This study offered a new approach for the development of low-melting-point composite materials.

1. Introduction

The Sn3.0Ag0.5Cu lead-free solder is considered a good interconnection material due to its excellent mechanical strength and reliability. It has widely used in ball grid array (BGA) packaging, wafer-level packaging, and three-dimensional (3D) packaging [1–3]. However, with the trend toward lightweight, miniaturized, and multifunctional of electronic products, microelectronic packaging is moving towards miniaturization and high density [4,5]. Consequently, the pitch and size of solder bumps have significantly reduced, demanding higher reliability of micro-solder joints. Traditional SnAgCu solders are no longer able to meet the requirements of future electronic packaging. Therefore, the development of a novel high-performance lead-free solder has become increasingly crucial.

To enhance the overall performance of SnAgCu solder, two primary approaches are commonly employed: micro-alloying and composite materials. Micro-alloying entails the addition of elements like Ni, Co, and Ce [6–8]. These alloying elements effectively improve solder's mechanical properties and wetting behavior by dissolving into the solder matrix, segregating at grain/phase boundaries, or forming precipitates. However, micro-alloying can introduce issues during prolonged service, such as the coarsening of precipitate phases, which compromises the reliability of solder joints [9]. Conversely, composite solders have garnered significant attention in recent years. Because the reinforcement does not react with the solder matrix and has no impact on the melting point. Incorporating nano-sized particles like TiO_2, SiC, CNTs [10–12] as reinforcements into the solder matrix is a popular strategy. Yet, the common challenges of nano-reinforcement particles

* Corresponding author.
** Corresponding author.
E-mail addresses: chenchuantong@sanken.osaka-u.ac.jp (C. Chen), zhkekekd@163.com (K. Zhang).

https://doi.org/10.1016/j.jmrt.2024.07.071
Received 25 February 2024; Received in revised form 5 July 2024; Accepted 14 July 2024
Available online 15 July 2024

aggregating and forming weak bonds at the interface with the solder matrix are hindering the development of composite solders.

The ideal development of a new solder material should involve the synergistic utilization of both the methods. For micro-alloying, a minimal quantity of metallic elements should be added, effectively preventing the coarsening of precipitate phases. Among the numerous alloying elements, rare earth metals are deemed "magical elements' for their ability to significantly enhance product quality and performance [13,14]. Among these rare earth elements, Ce has drawn attention. Ce belongs to the cubic crystal system alongside Sn, Ag, and Cu elements [15]. In terms of mechanical properties, Ce is relatively softer within the rare earth metals. It exhibits excellent ductility while sharing a hardness similar to that of Sn [16]. These characteristics render it compatible with SnAgCu solder in terms of crystal structure and mechanical performance. Additionally, Ce is an active element that contributes to improving the wettability of lead-free solders. Zhang et al. [17] reported that the addition of small amounts of Ce refined the microstructure of SnAgCu solder, reducing the thickness of intermetallic compounds (IMCs) at the interface. Wang et al. [18] investigated the influence of Ce during thermal cycling on the microstructure, wettability, and interface IMCs of SnAgCuBi solder alloys. The results indicate that the appropriate addition of Ce can refine the size of β-Sn, Ag_3Sn, and Cu_6Sn_5 in the solder alloy, enhancing its wettability and suppressing the growth rate of interfacial IMCs.

On the other hand, the selection of the reinforcing phase is also crucial in design of composite solder. Among the various reinforcing phases, graphene is considered an ideal reinforcing phase for fabricating electronic composite materials, due to its excellent thermal and electrical conductivity, high carrier mobility, and great specific surface areas [19], Liu et al. [20] reported that the addition of graphene refined the microstructure of Sn3.0Ag0.5Cu solder alloy and enhanced the tensile strength of the composite solder. Han et al. [21] prepared Ag particle-modified graphene reinforced Sn3.0Ag0.5Cu composite solder via powder metallurgy, refining the IMCs in the microstructure and improving the tensile strength. However, issues such as graphene's propensity for aggregation and weak bonding with the matrix metal significantly limit the preparation of graphene-reinforced composite lead-free solder. To address these concerns, surface modification is necessary. Commonly used Ni has a high binding energy with carbon-based nanomaterials [22,23] and can form a stable Ni_3Sn_4 phase with the solder matrix [24], thereby offering the potential for utilizing Ni-modified graphene as a reinforcing phase to prepare high-strength and tough composite lead-free solder. However, current surface metallization methods for graphene mainly involve electroless plating, which are associated with complex processes and may result in heavy metal ion contamination [25]. Furthermore, in the preparation process of metal-matrix composites, powder metallurgy is primarily employed, yet the powder metallurgy process for low melting point materials is currently immature. In addition, solid-state sintering is not conducive to the alloying of Ce elements within the solder matrix. Thus, exploring a simple, effective surface metallization method for graphene that exhibits good bonding with the matrix, along with an efficient process for preparing composite solder, has become crucial for achieving high-strength and tough composite solder.

In this study, Ni nanoparticle-modified reduced graphene oxide (Ni-rGO) was prepared by thermal decomposition method. The powder-melting method was first proposed to prepare Ni-rGO reinforced Sn2.5Ag0.7Cu0.1Ce composite solder. And the microstructure, wettability, electrical resistivity, and mechanical properties of Ni-rGO reinforced Sn2.5Ag0.7Cu0.1Ce composite solder were studied. This result is hoped to provide experimental basis for the development of graphene-reinforced lead-free composite solder.

2. Experimental procedure

2.1. Materials

Graphene oxide (GO) was purchased from Suzhou Co., China, with an average width of 5–15 μm and thickness of 5–25 nm. It was further reduced to obtain rGO through hydrazine hydrate reduction. In this study, rGO was used in place of graphene. On one hand, rGO has more surface functional groups and defects compared to graphene [26], which can serve as nucleation sites for subsequent modification with Ni nanoparticles. On the other hand, pure graphene is relatively expensive. In this research, rGO was obtained by reducing purchased GO with hydrazine hydrate, resulting in a more cost-effective solution. Sn2.5Ag0.7Cu solder powder, with particle sizes ranging from 25 to 48 μm, was provided by Changsha Co., China. The rare earth Ce was supplied by Henan University of Science and Technology.

2.2. Surface metallization of rGO

The rGO was ball-milled for 3 h within XQM-0.4L planetary ball mill. Subsequently, it was uniformly mixed with nickel acetate (Ni mole percentage of 10%). This mixture underwent heating at 500°C for 2 h in a tubular furnace under an H_2 atmosphere, resulting in Ni-rGO. The rGO and Ni-rGO were subjected to transmission electron microscope (TEM, JSM-2100, JEOL) analysis.

2.3. Preparation of Ni-rGO reinforced Sn2.5Ag0.7Cu0.1Ce composite solders

The powder-melting method was firstly proposed to prepare low-melting-point composite materials. Initially, the Sn2.5Ag0.7Cu solder powder was mixed with Ce powder at specified proportions using a QQM/B drum mixer for 10 h, yielding Sn2.5Ag0.7Cu0.1Ce solder alloy powder. Subsequently, this powder was mixed with various mass fractions of Ni-rGO (0, 0.01 wt%, 0.03 wt%, 0.05 wt%, and 0.1 wt%) in the drum mixer for 10 h. Then, mixed solder powder was packed into cylindrical-shaped alumina crucibles (ϕ20 mm) and heated in a muffle furnace at 250°C for 1 h under a N_2 atmosphere. Finally, the crucible containing the liquefied solder was air-cooled to obtain the Ni-rGO reinforced Sn2.5Ag0.7Cu0.1Ce composite solder. Additionally, Sn3.0Ag0.5Cu solder alloy was prepared using the same process as a reference.

The fabricated composite solder samples were polished, and the X-ray diffraction (XRD, D8 ADVANCE) analysis was conducted to confirm the phases. For microstructural observation, the solder alloys were etched using a 2 vol% HCl +98 vol% C_2H_5OH solution, followed by scanning electron microscopy (SEM, JSM-5610LV) observation and energy dispersive X-ray spectroscopy (EDS) analysis. Deep etching of the solder alloy was conducted for 10 h using a solution of 5 vol% HCl +3 vol% HNO_3 + 92 vol% CH_3OH, followed by 5 min of ultrasonication in alcohol solution. The three-dimensional morphology of the solder alloy microstructure was observed using SEM. The distribution of Ni-rGO was investigated with TEM equipped with EDS. The focused ion beam (FIB, FB-2100, Hitachi) was used to fabricate the TEM samples.

The electrical conductivity of the solder alloy was tested using a Sigma2008 B1 conductivity tester. Subsequently, the formula $\%IACS = (0.017241/\rho) \times 100\%$ was employed to calculate the resistivity. The result was the average of five measurements. The spread area of the solder was considered an indicator of the wettability. The wettability experiment was conducted according to the requirement of Chinese National Standard GB11364-2008 (solder spread-ability and caulking test method) [27]. 0.2 g of composite solder was placed on a cleaned Cu plate with flux (SR-12, SMIC, Japan), and heated to 270°C for 4 min. The spread area was measured, and the average was calculated from the results of five samples.

Schematic illustration of tensile specimen is shown in Fig. 1(a), with

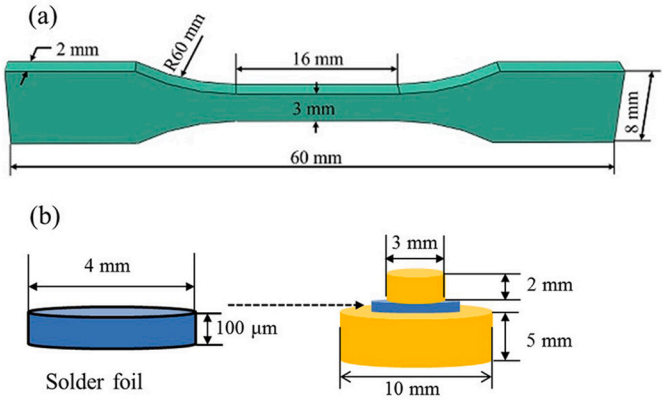

Fig. 1. Schematic illustration of (a) tensile specimen, and (b) solder joint.

a gauge length of 16 mm, length of 3 mm, and width of 2 mm. Tensile testing was performed at a rate of 1 mm/min using the universal testing machine (AG-I250 KN), and the average of five tensile results was taken as the experimental result. The tensile fracture surfaces were further examined using SEM, and the deformation-fracture mechanism was also investigated with TEM.

2.4. Soldering and thermal aging processes

The prepared solder blocks were rolled into foils with a thickness of 100 μm, and then cut into preforms with a diameter of 4 mm. The schematic diagram of the solder joint is shown in Fig. 1(b). The soldering process was carried out at 270°C for 4 min under a nitrogen atmosphere with flux (SR-12, SMIC, Japan). To evaluate the reliability of the newly developed composite solder, thermal aging tests on the solder joints were also conducted. The initial solder joints were subjected to thermal aging at 150°C for 500 h. Shear tests were conducted at a speed of 50 μm/s (ESR-4000, Nordson DAGE, UK). The shear strength was calculated as the average of five shear test results. The cross-sectional microstructure and shear fracture surfaces of the initial and thermally aged solder joints were observed using SEM.

3. Results and discussion

3.1. Surface metallization of rGO

Fig. 2 presents TEM, SAED, and HRTEM images of rGO before and after surface metallization. Fig. 2(a) shows the sheet-like structure of rGO with localized defects. It's attributed to the high-energy ball milling during the pre-treatment. The selected area electron diffraction (SAED) of area 1 in Fig. 2(a) is shown in Fig. 2(b), where the diffraction rings corresponding to rGO's (002) and (100) planes. The results indicate that localized damage to rGO during ball milling while maintaining its crystalline structure. Fig. 2(c) displays the HRTEM image of rGO where lattice fringes are visible, and the IFFT image of area 2 embedded in the upper right corner with lattice spacing of 0.342 nm, corresponding to the (002) plane of rGO. In addition, some curved lattice fringes and dislocations observed attribute to distortions and defects. These distortions and defects are caused by ball milling, potentially serving as nucleation sites for modifying metal particles like Ni [28].

Fig. 2(d) depicts TEM image of rGO after metallization, showing numerous dispersed nanoscale particles on its surface with an average size of 26.3 nm. To confirm the phase of these nanoparticles, SAED was conducted. Fig. 2(e) shows the SAED image of area 3 in Fig. 2(d), where the diffraction rings can be assigned to rGO's (002) plane and (111), (200), and (220) planes of Ni, confirming the presence of Ni nanoparticles. Fig. 2(f) shows the HRTEM image of Ni nanoparticles, with the IFFT image of area 4 in the upper right corner, exhibiting lattice spacing of 0.205 nm, corresponding to (111) plane of Ni. These results demonstrate that uniform loading of Ni nanoparticles occurs on the surface of rGO after surface modification, forming Ni-rGO, intended to be introduced into the solder matrix as reinforcement.

3.2. Microstructure of Ni-rGO reinforced Sn2.5Ag0.7Cu0.1Ce composite solders

Fig. 3 illustrates the XRD patterns of Sn3.0Ag0.5Cu (black line) and 0.05 wt% Ni-rGO reinforced Sn2.5Ag0.7Cu0.1Ce composite solder (blue line). For Sn3.0Ag0.5Cu, characteristic peaks of β-Sn are detected at 32.0°, 44.9°, 64.6°, and 89.4°, corresponding to the (101), (211), (321), and (431) planes of β-Sn, respectively. Additionally, characteristic peaks of Ag_3Sn are observed at 34.7°, 37.6°, and 39.6°, corresponding to the (020), (211), and (201) planes. The remaining peaks at 30.2°, 43.3°, and 79.1° correspond to the (101), (110), and (212) planes of Cu_6Sn_5. In the

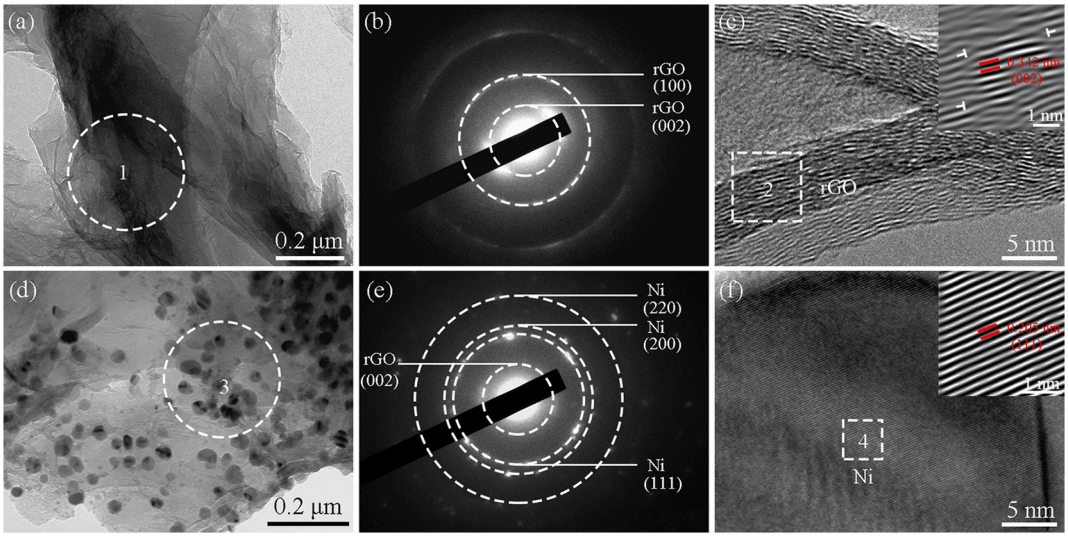

Fig. 2. TEM, SAED, and HRTEM images of rGO before and after surface metallization. (a) TEM image of rGO before surface metallization. (b) SAED of area 1 in Fig. 2 (a). (c) HRTEM image of rGO before surface metallization. (d) TEM image of rGO after surface metallization. (e) SAED of area 3 in Fig. 2(d). (f) HRTEM image of rGO after surface metallization.

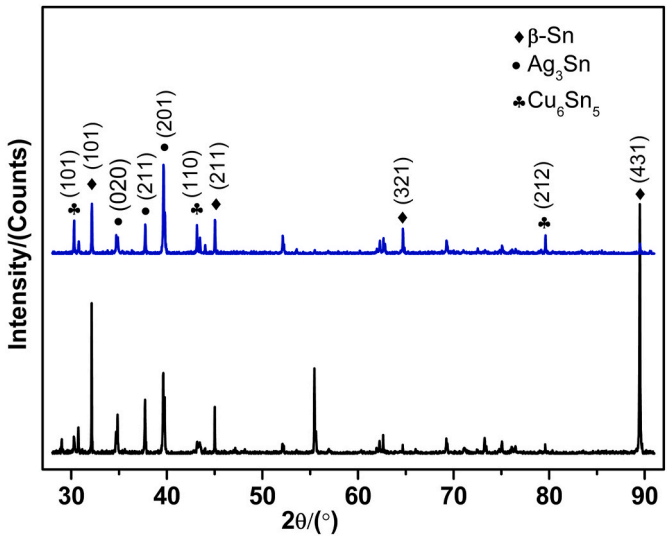

Fig. 3. XRD patterns of Sn3.0Ag0.5Cu (black line) and 0.05 wt% Ni-rGO reinforced Sn2.5Ag0.7Cu0.1Ce composite solder (blue line). (For interpretation of the references to color in this figure legend, the reader is referred to the Web version of this article.)

case of 0.05 wt% Ni-rGO reinforced Sn2.5Ag0.7Cu0.1Ce (blue line), the characteristic peaks almost appear at the same positions, also indicating the presence of β-Sn, Ag_3Sn, and Cu_6Sn_5 phases. However, an interesting phenomenon is observed that the intensities of some characteristic peaks have changed. Specifically, for composite solder, the intensities of the β-Sn characteristic peaks at 32.0° and 89.4° significantly decrease, while the intensities of the peaks at 40° for Ag_3Sn and 44° for Cu_6Sn_5 increase. These findings indicate an enhanced proportion of eutectic structures in the composite solder compared to Sn3.0Ag0.5Cu. Notably, the XRD pattern of composite solder does not show phases related to Ce, likely due to the low content of Ce element.

3.2.1. *Microstructure with shallow etching*

Fig. 4 illustrates the microstructures of Sn3.0Ag0.5Cu and Ni-rGO reinforced Sn2.5Ag0.7Cu0.1Ce composite solders. As observed in Fig. 4(a), the microstructure comprises primary β-Sn and eutectic microstructures. The eutectic encompasses granular β-Sn + Cu_6Sn_5, acicular β-Sn + Ag_3Sn binary eutectic, and β-Sn + Cu_6Sn_5 + Ag_3Sn ternary eutectic [29]. The shape of β-Sn appears non-uniform, including circular, elliptical, and elongated forms. This non-uniformity in the microstructure could negatively impact the performance [30]. The shape of the IMCs in the eutectic includes granular and short rod-like, and their formation had been systematically studied in previous research [31]. When the composition of the solder alloy is changed to Sn2.5Ag0.7Cu (Fig. 4(b)), the proportion of the eutectic structure decreases. It is attributed to the reduced Ag content. An interesting phenomenon occurs when 0.1 wt% Ce is added. As shown in Fig. 4(c), when the solder alloy composition becomes Sn2.5Ag0.7Cu0.1Ce, the proportion of the eutectic structure increases. This result indicates that the addition of Ce elements can significantly improve the microstructure of the solder alloy, increasing the proportion of the eutectic structure. Furthermore, the shape and size of the β-Sn phase change compared to Sn2.5Ag0.7Cu. Moreover, there are changes in the shape and size of β-Sn compared to Sn3.0Ag0.5Cu. The average size of β-Sn decreased to 41.5 μm, gradually becoming more uniform and tending toward elliptical shapes, without observing large-sized β-Sn.

On this basis of Sn2.5Ag0.7Cu0.1Ce solder alloy, Ni-rGO was introduced. Overall, with the addition of Ni-rGO, the proportion of eutectics is increased. And the size of β-Sn particles tends to gradually decrease, and the shape transitions from elliptical to circular. The microstructure becomes more uniform and significantly refined. When the amount of Ni-rGO added reached 0.01 wt% (Fig. 4(d)), β-Sn appears mostly elliptical with a few circular forms, exhibiting good size uniformity. At this stage, β-Sn measured of 35.5 μm. Moreover, the size of IMC particles in the eutectic structures also reduced to 2.1 μm. As the content of Ni-rGO

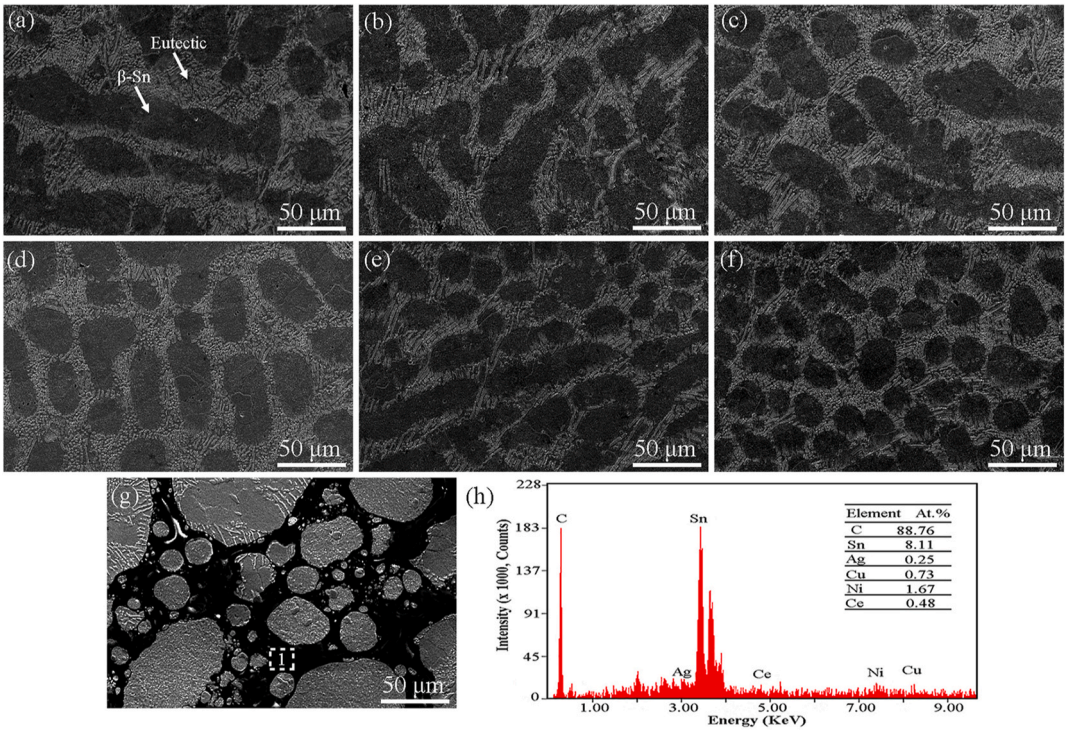

Fig. 4. Microstructures of Sn3.0Ag0.5Cu and Ni-rGO reinforced Sn2.5Ag0.7Cu0.1Ce composite solders. (a) Sn3.0Ag0.5Cu, (b) Sn2.5Ag0.7Cu, (c) Sn2.5Ag0.7-Cu0.1Ce. Composite solders with (d) 0.01 wt% Ni-rGO, (e) 0.03 wt% Ni-rGO, (f) 0.05 wt% Ni-rGO, (g) 0.1 wt% Ni-rGO addition, respectively. (h) EDS analysis of area 1 in Fig. 4(f).

increased, the size of β-Sn gradually diminished, and the proportion of circular β-Sn further increased. At 0.05 wt% addition of Ni-rGO (Fig. 4 (f)), the composite solder demonstrates a uniform and refined microstructure. Here, almost all β-Sn consists of circular forms, with the size of 20.7 μm, making a 50.1% reduction compared to the absence of Ni-rGO, with reduced IMC sizes as well. However, at 0.1 wt% addition (Fig. 4 (g)), the uniform and refined microstructure vanishes, and the black phase is observed on the surface of the composite solder's microstructure. EDS analysis of area 1 in Fig. 4(g) (shown in Fig. 4(h)) reveals the presence of C and Ni, indicating the aggregated black material as Ni-rGO. A small amount of the rare earth element Ce is also detected, further indicating the effective addition of the Ce into the solder matrix.

The above results indicate that the appropriate addition of Ce and Ni-rGO can effectively improve the microstructure of the solder, although the refinement mechanisms differ. For the effect of Ce, adding an appropriate amount of Ce increases the undercooling of the liquid solder, providing more nucleation sites for the primary β-Sn phase and the eutectic structure [32,33]. Furthermore, according to the Sn–Ce phase diagram, the addition of rare earth elements results in the formation of $CeSn_3$ compounds, which are dispersed near grain boundaries and phase boundaries [34]. These compounds exert a pinning effect that inhibits grain boundary migration, refining the microstructure of the solder alloy through the two mechanisms. For Ni-rGO induced composite solder microstructure refinement, it can be explained thermodynamically and kinetically. During the growth of solder grains, grain boundary migration occurs continuously, driven by the reduction of interfacial energy [35]. As the thinnest two-dimensional material, rGO has an extremely high specific surface area. When Ni-rGO is added to the solder alloy, it increases the system's interfacial energy, thus reducing the driving force for grain boundary diffusion and inhibiting grain growth [36]. Additionally, Ni-rGO, distributed along the grain boundaries, provides a pinning effect that obstructs further grain growth. Consequently, with the increasing amount of the reinforcing phase, the grain size gradually decreases.

In summary, the addition of Ni-rGO significantly alternate the microstructure of the composite solder, which consequently affects the solder's performance. To further explore the impact of Ni-rGO addition on the microstructure of the composite solder, a deep etching experiment was also conducted.

3.2.2. Microstructure with deep etching

The deep etching SEM images of Sn2.5Ag0.7Cu0.1Ce solder and 0.05 wt% Ni-rGO reinforced Sn2.5Ag0.7Cu0.1Ce composite solder are shown in Fig. 5. Fig. 5(a)–(d) represent the SEM images of the Sn2.5Ag0.7Cu0.1Ce solder alloy. As observed in Fig. 5(a), the Sn2.5Ag0.7Cu0.1Ce solder alloy exhibits a three-dimensional morphology. In the eutectic regions, β-Sn is corroded away, leaving behind Ag_3Sn and Cu_6Sn_5 IMCs. Fig. 5(b) presents the middle-magnification SEM image of β-Sn, revealing that the primary β-Sn displays a laminar striped morphology after deep etching. This phenomenon is first reported. Additionally, dispersed particles are observed adhering to the sheet-like Ag_3Sn, confirmed as Cu_6Sn_5 phase by EDS analysis of point A (shown in Table 1). This occurs because, similar to Ag, Cu scarcely dissolves in β-Sn but forms Cu–Sn intermetallic compound Cu_6Sn_5, attaching to the sheet-like Ag_3Sn for nucleation and growth [37]. Fig. 5(c) illustrates the middle-magnification SEM image of the IMCs of the eutectics. It shows predominantly needle-like Ag_3Sn and minor sheet-like Ag_3Sn. The high-magnification SEM image of Sn2.5Ag0.7Cu0.1Ce solder is presented in Fig. 5(d), displaying particles of varying sizes mounted on needle-like Ag_3Sn, confirmed as Cu_6Sn_5 by EDS analysis of point B (shown in Table 1). In addition, on the surface of sheet-like Ag_3Sn, perpendicular striped lines are observed, and Cu_6Sn_5 particles are also attached at the surface and edges of the sheet-like Ag_3Sn.

Fig. 5(a1)-(d1) depict the deep etching SEM images of the 0.05 wt% Ni-rGO reinforced Sn2.5Ag0.7Cu0.1Ce composite solder. Fig. 5(a1) shows a low-magnification SEM image, similar to Fig. 5(a), where β-Sn within the eutectic structure is corroded, revealing a three-dimensional IMC. The size of the primary β-Sn in the composite solder is smaller than that in the Sn2.5Ag0.7Cu0.1Ce solder alloy, consistent with the results in Fig. 4. Fig. 5(b1) displays the middle-magnification SEM image of β-Sn in the composite solder, also illustrating laminar β-Sn, indicating the layered crystalline growth of β-Sn. Further investigation is needed in the future. The middle-magnification SEM image of the IMCs within the eutectic structure of the composite solder is depicted in Fig. 5(c1). Unlike Sn2.5Ag0.7Cu0.1Ce, the eutectic structure in the composite solder primarily exists in sheet-like form, with some Ag_3Sn displaying elliptical and elongated pores. The high-magnification SEM image of the composite solder is shown in Fig. 5(d1), presenting an abundance of fine particles at the edges of sheet-like Ag_3Sn, giving it a coral-like appearance. Sn, Ag, Cu, and Ni elements are detected via EDS in point C (shown in Table 1). These Ni elements originate from the reinforcing phase Ni-rGO, indicating the effective addition of Ni-rGO into the solder matrix. However, rGO was not detected at this stage, potentially due to its removal during the ultrasonic cleaning process of the deep etching.

During the non-equilibrium solidification process of the liquid

Table 1
EDS results of deep etching solders (At.%).

Location	Sn	Ag	Cu	Ni
A	31.15	52.53	16.32	0
B	39.82	37.52	22.66	0
C	38.71	37.20	21.53	2.56

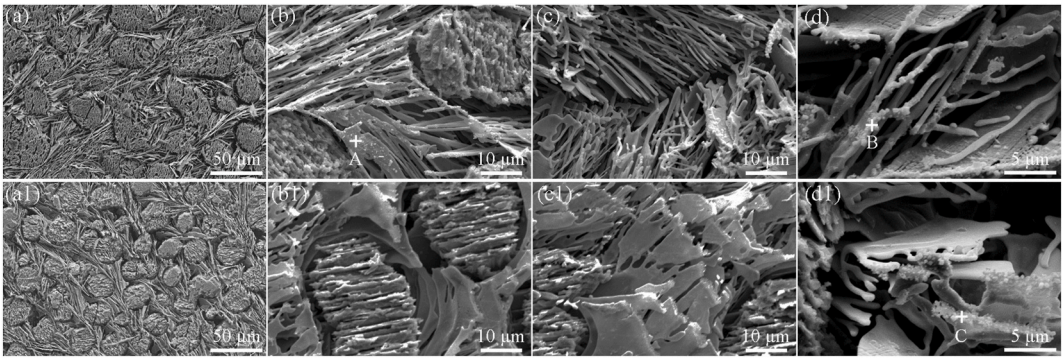

Fig. 5. Deep etching SEM images of Sn2.5Ag0.7Cu0.1Ce solder and 0.05 wt% Ni-rGO reinforced Sn2.5Ag0.7Cu0.1Ce composite solder. Low-magnification SEM image of (a) Sn2.5Ag0.7Cu0.1Ce solder, and (a1) composite solder. Middle-magnification SEM image of β-Sn in (b) Sn2.5Ag0.7Cu0.1Ce solder, and (b1) composite solder. Middle-magnification SEM image of IMCs of the eutectics in (c) Sn2.5Ag0.7Cu0.1Ce solder, and (c1) composite solder. High-magnification SEM image of (d) Sn2.5Ag0.7Cu0.1Ce solder, and (d1) composite solder.

solder, Ag_3Sn crystal nuclei formed at the beginning of the reaction preferentially oriented and grew into a needle-like phase [38]. As solidification progressed, the eutectic Ag_3Sn phase grew attached to the surface of the primary Ag_3Sn phase, in which sheet-like eutectic Ag_3Sn was formed [39]. This is the reason why both needle-like and sheet-like Ag_3Sn phases can be observed in Fig. 5(c). With the addition of 0.05 wt% Ni-rGO, an increased percentage of sheet-like Ag_3Sn is observed. This is due to graphene being a two-dimensional material with an exceptionally high specific surface area. During the solidification process of Ag_3Sn, Ni-rGO acts as nucleation sites for Ag_3Sn, prompting the attachment and growth of Ag_3Sn onto Ni-rGO, ultimately presenting a higher proportion of sheet-like phases. These sheet-like Ag_3Sn structures, within the Sn matrix, act as in situ-generated reinforcing phases. Compared to the needle-like Ag_3Sn, the sheet-like Ag_3Sn provides a larger contact area with the Sn matrix, enhancing load transfer effects. This positively contributes to improving the mechanical properties of the solder.

3.2.3. TEM of 0.05 wt% Ni-rGO reinforced Sn2.5Ag0.7Cu0.1Ce composite solder

To further explore the effect of Ni-rGO in the microstructure of the composite solder, TEM observation was conducted. Fig. 6(a) shows the TEM image of the composite solder, revealing clear grain boundaries. And numerous dark-phase particles are observed along the grain boundaries, corresponding to the EDS results are displayed in Fig. 6(d)–(f) and Fig. S1. And Fig. S1 shows the EDS mapping of Ni element. Due to the very low concentration of Ni and the resolution limitations of EDS, it is challenging to determine the presence of Ni elements through EDS analysis. The results indicate that these dark-phase particles contain Ag_3Sn and Cu_6Sn_5. Some are isolated Ag_3Sn, formed during the solidification process as β-Sn + Ag_3Sn binary eutectics. Others represent interdependence between Ag_3Sn and Cu_6Sn_5, indicating the formation of β-Sn + Ag_3Sn + Cu_6Sn_5 ternary eutectics during solidification. These IMCs form at the grain boundaries, attributed to higher free energy at the grain boundaries compared to within the grains. However, intriguingly, for the region on the far right in Fig. 6(a), its EDS results do not entirely match. Part of the area (marked by the red dashed line) lacks detected Ag or Cu elements. To identify this specific area, SAED was performed. Fig. 6(c) displays the SAED of area 2 in Fig. 6(b), identified as the (002) plane of rGO and the (111) and (220) planes of Ni. This confirms that the region marked by the red dashed line in Fig. 6(b) corresponds to Ni-rGO. These results confirm the effective addition of Ni-rGO into the solder matrix. Characterizing graphene in metal-matrix composites has been challenging, even doubted whether it can be effectively incorporated into the matrix. However, in this study, Ni-rGO was detected, indicating its successful addition into the solder matrix. The result breaks the technical difficulty that graphene cannot be effectively added to low melting point metals. This success is attributed, on one hand, to the surface modification of graphene. Surface modification with Ni nanoparticles improved not only the density difference with the solder matrix but also enhanced the interface bonding between graphene and the solder matrix. On the other hand, this success is attributed to the powder-melting method proposed in this study. Additionally, Fig. 6(b) demonstrates that Ni-rGO is positioned at triple junctions grain boundary, where ternary eutectics attach to Ni-rGO nuclei. Furthermore, numerous dislocations are observed near the grain boundaries due to the mismatch in thermal expansion coefficients between β-Sn, IMCs and reinforcing phases.

3.3. Wettability of Ni-rGO reinforced Sn2.5Ag0.7Cu0.1Ce composite solder

The spreading areas of Sn2.5Ag0.7Cu0.1Ce composite solder reinforced with various addition amounts of Ni-rGO on Cu substrate are

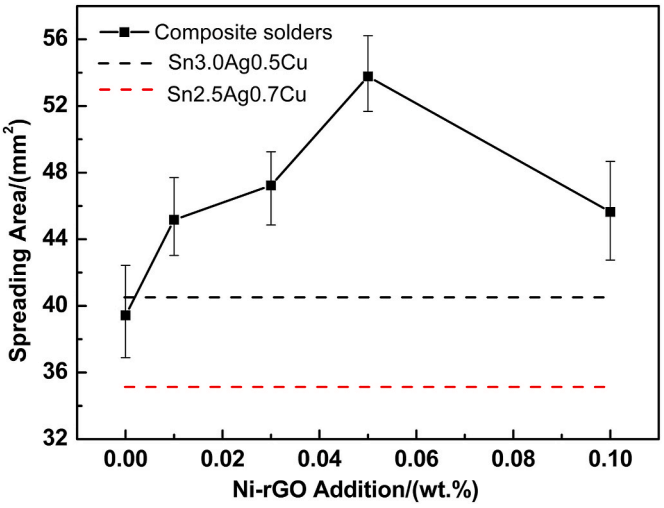

Fig. 7. The spreading areas of Sn2.5Ag0.7Cu0.1Ce composite solder reinforced with various addition amounts of Ni-rGO on Cu substrate.

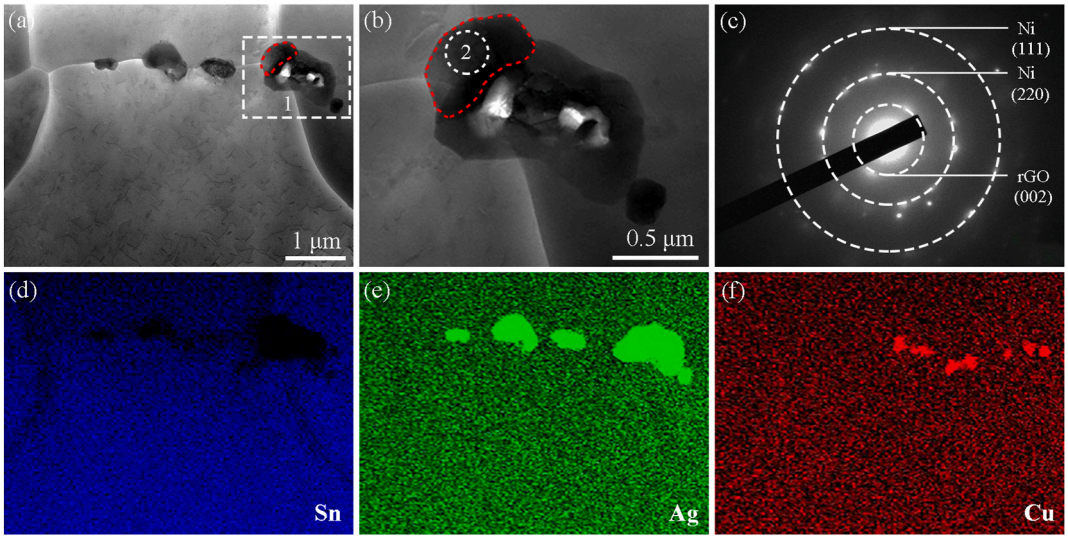

Fig. 6. TEM, SAED, and EDS images of 0.05 wt% Ni-rGO reinforced Sn2.5Ag0.7Cu0.1Ce composite solder. (a) TEM image. (b) High-magnification view of area 1 in Fig. 6(a). (c) SAED of area 2 in Fig. 6(b). EDS maps of (d) Sn, (e) Ag, and (f) Cu elements of Fig. 6(a).

illustrated in Fig. 7. The red dashed line in Fig. 7 represents the spread area of Sn2.5Ag0.7Cu solder, which is 35.1 mm^2. After adding 0.1 wt% Ce, the spread area of Sn2.5Ag0.7Cu0.1Ce solder increases to 39.4 mm^2, representing a 12.3% improvement compared to the solder without Ce. These results indicate that the addition of Ce can enhance the solder's wettability. However, the spread area of Sn2.5Ag0.7Cu0.1Ce solder is still lower than that of commercial Sn3.0Ag0.5Cu solder (indicated by the black dashed line in Fig. 7). Therefore, Ni-rGO is added to further improve the wettability. As the amount of the Ni-rGO increases, the spread area of the composite solder initially increases and then decreases.

At an addition amount of 0.01 wt%, the spreading area reaches 45.2 mm^2, surpassing the spreading area of 40.5 mm^2 for Sn3.0Ag0.5Cu solder. When the Ni-rGO addition reaches 0.05 wt%, the spreading area researches the maximum value of 53.8 mm^2, marking a 36.5% increase compared to Sn2.5Ag0.7Cu0.1Ce. However, further increasing the Ni-rGO addition to 0.1 wt% causes the spreading area to decrease to 46.6 mm^2, yet it remains higher than that of Sn3.0Ag0.5Cu solder.

During the spreading process of liquid-state solder, Ni-rGO exhibits an adsorption effect on the surface of the liquid-state solder, based on the Gibbs adsorption formula [40].

$$\Gamma = -\frac{C}{RT}\left(\frac{d\sigma}{dC}\right)_T \tag{1}$$

where Γ is the adsorption capacity; C is the concentration of Ni-rGO; σ is the surface tension, N/m; T is the Kelvin temperature, K; R is the gas constant, 8.314.

Convert formula (1) to get formula (2):

$$-\Gamma\frac{RT}{C} = \left(\frac{d\sigma}{dC}\right)_T \tag{2}$$

Integrate formula (2) to get formula (3):

$$-RT\int\frac{\Gamma}{C}dC = \sigma - \sigma_0 \tag{3}$$

$$\text{That is}: \sigma = \sigma_0 - RT\int\frac{\Gamma}{C}dC \tag{4}$$

where σ_0 is the surface tension without Ni-rGO addition.

Since Ni-rGO is positively adsorbed, so $\Gamma > 0$.

That is, with the addition of Ni-rGO, the surface tension of the liquid solder decreases.

$$\cos\theta = \frac{\sigma_{sg} - \sigma_{sl}}{\sigma_{lg}} \tag{5}$$

According to formula (5), when the surface tension of the liquid-state solder decreases (σ_{lg}), the wetting angle θ decreases, resulting in a larger spreading area of the solder. However, with a further increase in the addition of Ni-rGO, the spreading area decreases instead. This is attributed to the continuous addition of Ni-rGO, which increases the viscosity of the liquid-state solder. Similar result was also reported in Ref. [41].

3.4. Electrical resistivity of Ni-rGO reinforced Sn2.5Ag0.7Cu0.1Ce composite solder

The electrical resistivity of Ni-rGO reinforced Sn2.5Ag0.7Cu0.1Ce composite solder is shown in Fig. 8. The red dashed line in Fig. 8 represents the resistivity of Sn2.5Ag0.7Cu solder, which is 11.7 μΩ cm. When 0.1 wt% Ce is added, its resistivity slightly increases to 12.0 μΩ cm. This increase is attributed to the partial dissolution of Ce into the solder matrix and the formation of $CeSn_3$ IMCs [34], both of which contribute to the increase in resistivity. Building on the Sn2.5Ag0.7Cu0.1Ce base, Ni-rGO was subsequently added. As the amount of Ni-rGO increases, the resistivity shows a gradual upward trend. When the

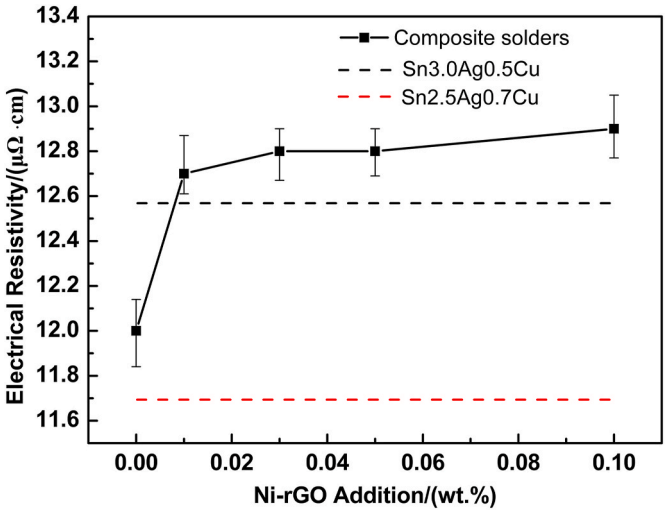

Fig. 8. The electrical resistivity of Sn2.5Ag0.7Cu0.1Ce composite solder reinforced with various addition amounts of Ni-rGO.

Ni-rGO addition is 0.01 wt%, the resistivity increases to 12.7 μΩ cm. Further increasing the Ni-rGO content to 0.1 wt% raises the resistivity to 12.9 μΩ cm. This is because Ni-rGO is dispersed within the solder matrix, which affects electron scattering and thus increases resistivity. However, due to the relatively low addition amount, the increase in resistivity is limited. Therefore, the resistivity of the composite solder falls within the range of 12.0–12.9 μΩ cm, it remains almost consistent with the resistivity of Sn3.0Ag0.5Cu. Similar conclusions were also drawn by Ismail et al. [42]. In addition, the results of composite solder were lower than that of Sn37Pb solder with 14.5 μΩ cm [43], exhibiting application prospects in electronic packaging.

Electrical resistivity is an intrinsic property of a conductive material, describing the resistance to electric current flow per unit length and unit cross-sectional area. Different materials exhibit varying resistivities, which are inherent attributes independent of the conductor's size and shape. Higher resistivity indicates greater resistance to current flow, whereas lower resistivity signifies better conductivity. On a microscopic level, for pure metals (where impurities and defects can be neglected), resistivity mainly arises from electron scattering due to lattice vibrations [44], which is temperature dependent. However, in practical materials, impurities and defects are present. The periodic potential field and causing electron scattering are disrupted. Generally, in metallic materials, the effect of impurities and defects is temperature-independent but directly proportional to their concentration [45]. Consequently, any factor influencing electron scattering will alter the material's resistivity. According to Matthiessen's rule, the total resistivity of a conductive material consists of the following components [46]:

$$\rho_{total} = \rho_0 + \rho_{doping} + \rho_{thermal} + \rho_{deform}$$

where ρ_{total} is the total resistivity of the material, ρ_0 is the initial resistivity, ρ_{doping} is the resistivity due to doping, $\rho_{thermal}$ is the resistivity due to temperature, and ρ_{deform} is the resistivity due to deformation.

In this study, for the Ni-rGO reinforced Sn2.5Ag0.7Cu0.1Ce composite solder, all specimens were prepared using the same process, without plastic deformation, and electrical characteristics were tested at room temperature. Therefore, $\rho_{thermal}$ and ρ_{deform} can be neglected, meaning the composite solder's resistivity is primarily due to ρ_{doping}. And ρ_{doping} is mainly attributed to two factors: the dissolution of Ce into the Sn2.5Ag0.7Cu solder matrix and the presence of the reinforcement phase Ni-rGO. The dissolution of Ce into the solder matrix, along with the formation of $CeSn_3$ IMC, influences electron scattering, thereby altering the resistivity. Meanwhile, Ni-rGO acts as a dispersed phase,

also affecting electron scattering and leading to changes in resistivity.

3.5. Mechanical properties of Ni-rGO reinforced Sn2.5Ag0.7Cu0.1Cecomposite solders

3.5.1. Tensile properties of composite solders

The tensile strength and elongation of Sn2.5Ag0.7Cu0.1Ce composite solders reinforced with various Ni-rGO contents are depicted in Fig. 9. With an increase in Ni-rGO content, the tensile strength of composite solders initially increases and then decreases, while the corresponding elongation exhibits a gradual decrease. The tensile strength of Sn2.5Ag0.7Cu solder is 45.3 MPa (indicated by the red horizontal solid line), with a corresponding elongation of 48.2% (blue horizontal solid line). When 0.1 wt% Ce is added, the tensile strength increases to 50.5 MPa, an 11.5% increase compared to the solder without Ce element. This is because an appropriate amount of Ce in the solder matrix acts as a nucleation site for β-Sn and eutectic microstructures, resulting in grain refinement and consequent strengthening. It has already corroborated by the SEM images in Fig. 4. Additionally, the inclusion of Ce forms $CeSn_3$ phases [34], contributing to dispersion strengthening. With the addition of Ni-rGO, the tensile strength further increases. At a Ni-rGO content of 0.01 wt%, the tensile strength reaches 52.3 MPa, with a corresponding elongation of 39.1%. As the Ni-rGO content increases, the tensile strength continues to rise, while elongation gradually decreases. When the Ni-rGO content is 0.05 wt%, the tensile strength peaks at 58.1 MPa, a 15.0% improvement over Sn2.5Ag0.7Cu0.1Ce, with the composite solder exhibiting an elongation of 33.8%. The enhancement in the composite solder's performance can be attributed to microstructural refinement, as illustrated in Fig. 4. The addition of Ni-rGO leads to a refined microstructure, which enhances the mechanical properties of the composite solder. Furthermore, Ni-rGO, as a nano-reinforcement, is dispersed within the solder matrix, inducing the Orowan strengthening mechanism, thereby increasing the tensile strength. Ni-rGO, being a two-dimensional material, also exhibits excellent load transfer effects, further enhancing the tensile strength of the composite solder. However, when the Ni-rGO content is increased to 0.1 wt%, the tensile strength decreases to 51.3 MPa, and the elongation drops to 30.2%. This reduction is attributed to the agglomeration of the reinforcement phase, as noted in Fig. 4(g), which diminishes the strengthening effect of the reinforcement.

In summary, at 0.05 wt% Ni-rGO addition, the composite solder exhibits An UTS and elongation of 58.1 MPa and 33.8%, respectively, surpassing the tensile strength of Sn3.0Ag0.5Cu solder alloy prepared under the same processing conditions. The result also higher than that of the GNS enhanced Sn3.0Ag0.5Cu composite solder prepared in Ref. [20]

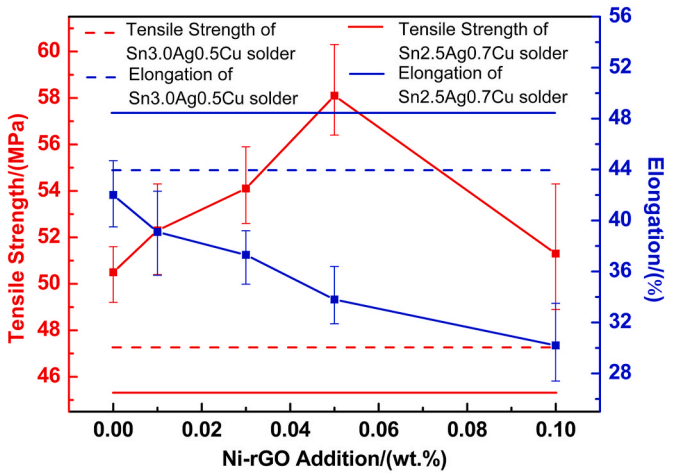

Fig. 9. The tensile strength and elongation of Sn2.5Ag0.7Cu0.1Ce composite solders reinforced with various addition amounts of Ni-rGO.

and significantly outperform the tensile strength of commercial Sn3.0Ag0.5Cu solder via traditional casting methods [47], signifying the achievement of a high-strength and tough Ni-rGO reinforced Sn2.5Ag0.7Cu0.1Ce composite solder.

The fracture surface of the composite solder is illustrated in Fig. 10. Fig. 10(a) shows the fracture morphology of the Sn3.0Ag0.5Cu solder alloy, presenting a ductile fracture dominated by dimples. With the addition of Ce and varying amounts of Ni-rGO, the number and size of dimples decrease, while cleavage increases. The fracture mechanism transitions from predominantly ductile fracture dominated by dimples to a ductile-brittle mixed fracture characterized by dimples and cleavage surfaces. The EDS results for point A and B in Fig. 11(a) are presented in Table 2, revealing that region A consists of β-Sn, while the primary compositions of region B are eutectics. In region A, the fracture mechanism of β-Sn exhibits dimple fracture, whereas the fracture of eutectic regions involves dimple fracture of β-Sn and cleavage fracture of the IMCs Ag_3Sn and Cu_6Sn_5. As mentioned in Figs. 3 and 4, the proportion of eutectics in the Sn3.0Ag0.5Cu solder alloy is relatively low, resulting primarily in a ductile fracture. The fracture morphology of Sn2.5Ag0.7Cu is shown in Fig. S2. It also exhibits typical ductile fracture characteristics. Additionally, the proportion of eutectic structure on the fracture surface is lower than that in Fig. 10(a), which is attributed to the reduced Ag content. With an increase in Ni-rGO addition content, there is a reduction in the number and size of dimples and an increase in cleavage surfaces in the fracture. The EDS results for points C and D in Fig. 10(e) are presented in Table 2, revealing region C as β-Sn and the region D consist of Ag_3Sn and Cu_6Sn_5. This refinement of primary β-Sn structures and an increase in eutectic structures due to the addition of Ce and Ni-rGO lead to an increased proportion of eutectics comprising brittle phases such as Ag_3Sn and Cu_6Sn_5. As the eutectics increase, the proportion of cleavage surfaces in the fracture also increases, leading to a fracture mode characterized by a mixture of dimples and cleavage surfaces. Upon increasing the Ni-rGO content to 0.1 wt%, the proportion of cleavage surfaces further increases, accompanied by larger cleavage surfaces.

To further investigate the deformation-fracture mechanisms during the tensile process, localized regions of fractured sample was selected for TEM observation. Initially, FIB machining was employed in area 1 of Fig. 10(e) to prepare the TEM sample. The TEM images are depicted in Fig. 11. Fig. 11(a) displays TEM images of the fractured surface of the composite solder, revealing various types of dislocations. Short dislocations in area 1, long dislocations in area 2, and dislocation pileups in area 3 are observable. As known, plastic deformation generates dislocations in the tensile process, including Frank-Read dislocation sources [48], continuously increasing their quantity during elongation of the composite solder. The long dislocations in Fig. 11(a) are the result of the joint action of dislocation proliferation and dislocation delivery. As tensile deformation progresses, many dislocations encountering obstacles such as Ag_3Sn, Cu_6Sn_5, Ni-rGO, and grain boundaries impedes their movement, leading to blockage and accumulation of dislocations. Area 3 in Fig. 11(a) shows dislocation pileups restrained by grain boundaries. Similarly, in Fig. 11(b), several precipitate phases can be observed, among which, the SAED in area 4, located in the bottom right corner, corresponds to the $(\bar{1}2\bar{1})$, (121), and (040) planes of Ag_3Sn along the $[\bar{4}04]$ axis. Dislocation pileups are also observed under the influence of these IMCs. Additionally, entanglement and accumulation of dislocations lead to the formation of dislocation walls [49], as illustrated in Fig. 11(c). These accumulations create significant stress concentration in the obstacle zones. If the local stress concentration surpasses the material's critical fracture strength, microcracks are initiated. Under continued external stress, the size and number of these microcracks progressively increase, resulting in the fracture of the composite solder, as depicted in the fracture surface in Fig. 10.

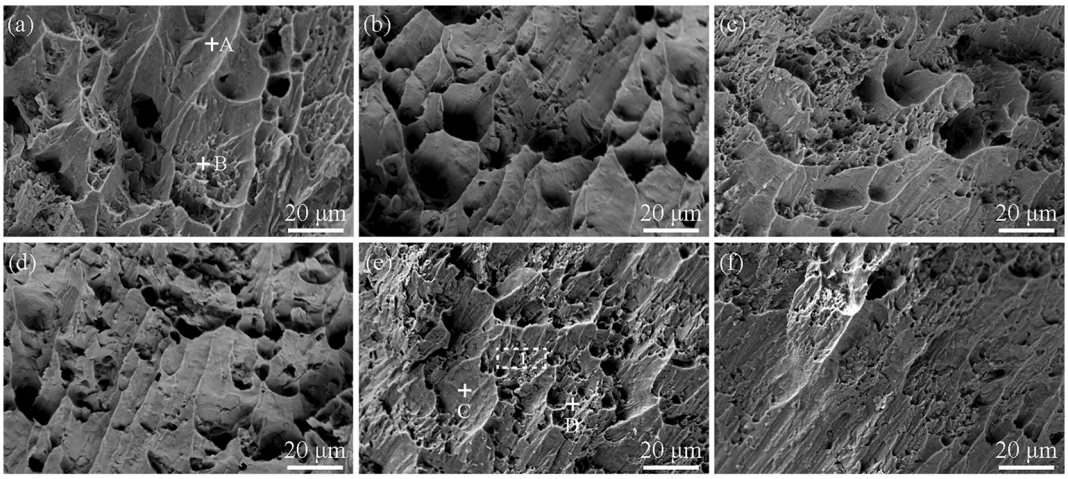

Fig. 10. Fracture surfaces of Sn3.0Ag0.5Cu and Ni-rGO reinforced Sn2.5Ag0.7Cu0.1Ce composite solders. (a) Sn3.0Ag0.5Cu, (b) Sn2.5Ag0.7Cu0.1Ce. Composite solders with (c) 0.01 wt% Ni-rGO, (d) 0.03 wt% Ni-rGO, (e) 0.05 wt% Ni-rGO, (f) 0.1 wt% Ni-rGO addition, respectively.

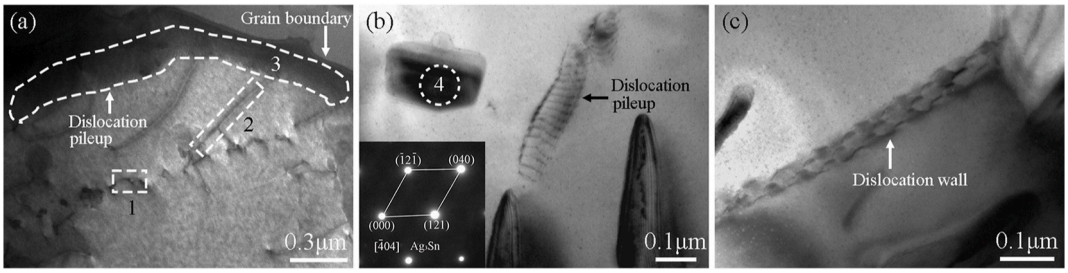

Fig. 11. TEM images of fractured sample of 0.05 wt% Ni-rGO reinforced Sn2.5Ag0.7Cu0.1Ce composite solder. Dislocation pileups at (a) grain boundary, (b) IMCs. (c) Dislocation wall.

Table 2
EDS results of fracture surface of composite solders (At.%).

Location	Sn	Ag	Cu
A	92.10	3.41	4.49
B	55.69	31.52	12.79
C	92.95	3.46	3.59
D	58.37	28.13	13.50

3.5.2. Strengthening mechanism of Ni-rGO reinforced Sn2.5Ag0.7Cu0.1Ce composite solders

The improvement of mechanical properties of Ni-rGO reinforced Sn2.5Ag0.7Cu0.1Ce composite solder mainly attributes to three aspects.

3.5.2.1. Load transfer strengthening mechanism. Analyzing the composite solder using the shear lag model [50]. This model is based on the well bonded interface between the solder matrix and Ni-rGO, transferring loads through interfacial shear stress between the solder matrix and Ni-rGO. In this study, surface metalized rGO showed a good bond with the solder matrix, favoring enhanced load transfer effect, thus elevating the solder's tensile strength. Moreover, due to the addition of Ni-rGO, the transformation of needle-like Ag_3Sn to sheet-like Ag_3Sn in the eutectics (as shown in Fig. 5) increased the contact area between the sheet-like Ag_3Sn and the Sn matrix, also promoting a better load transfer effect. Based on this model, the strength of the composite solder can be expressed as formula (7) [51]:

$$\sigma_{L.T} = 0.5 \bullet \sigma_m \bullet V_r \bullet \frac{l}{d} \tag{7}$$

where $\sigma_{L.T}$ is the strengthening effect caused by load transfer strengthening mechanism, σ_m is the strength of the solder matrix, V_r is the volume fraction of reinforcement Ni-rGO, and $\frac{l}{d}$ is the aspect ratio of the graphene.

According to formula (7), the increase in $\sigma_{L.T}$ primarily depends on the volume fraction f of the reinforcement Ni-rGO and the aspect ratio of the graphene. When V_r is greater, $\sigma_{L.T}$ is higher. Within a certain range, $\sigma_{L.T}$ also increases with an increase in V_r, but excessively high-volume fractions can lead to reinforcement agglomeration, ultimately reducing the strength of the composite solder.

3.5.2.2. Orowan strengthening mechanism. Graphene, as the strongest and hardest material with a thickness at the nanometer level, is an ideal candidate for Orowan strengthening. In this study, Ni-rGO was uniformly introduced into the SnAgCu solder alloy matrix via powder-melting method. During the deformation process of the composite solder, Ni-rGO impedes dislocation motion, causing dislocations to bend and generate back stress, further hindering dislocation motion until the dislocation lines bypass the reinforcing phase to continue advancing. This can be qualitatively explained by formula (8) [52].

$$\sigma_{Orowan} = \frac{0.13 \bullet G_m \bullet b}{d_r \bullet \left(\sqrt[3]{\frac{1}{2V_r}} - 1\right)} \bullet \ln\left(\frac{d_r}{2b}\right) \tag{8}$$

where σ_{Orowan} is the strengthening effect caused by the Orowan strengthening mechanism, G_m is the shear modulus of the solder matrix alloy, d_r is the size of reinforcement Ni-rGO, b is the Burgers vector of the solder matrix, and V_r is the volume fraction of Ni-rGO.

3.5.2.3. Grain refinement strengthening mechanism. The refinement of grains can simultaneously improve the strength and plasticity of

composite solder. As mentioned in Fig. 4, the addition of Ce and Ni-rGO effectively refined the size of β-Sn and IMC. This improved strength due to microstructure refinement can be explained by the Hall-Petch formula [53]:

$$\sigma_{G.R} = k \bullet \left(d^{-0.5} - d_0{}^{-0.5}\right) \tag{9}$$

where $\sigma_{G.R}$ is the strengthening effect caused by the grain refinement mechanism, k is a constant, d is the grain size of the composite soler, and d_0 is the grain size of the plain solder.

3.5.2.4. Thermal mismatch dislocation strengthening mechanism. There is a significant difference in the CTE between the solder matrix and GNS the CTE of SnAgCu is approximately 21.6×10^{-6}/K, while that of GNS is approximately 1.0×10^{-6}/K [26], leading to noticeable thermal mismatch phenomena, thereby causing an increase in dislocation density in the composite solder. The expression for dislocation density is shown in formula (10) [54]:

$$\sigma_{T.M} = k \bullet G_m \bullet b \bullet \sqrt{\frac{12 \bullet \Delta\alpha \bullet \Delta T \bullet V_r}{b \bullet d_r \bullet (1 - V_r)}} \tag{10}$$

where $\sigma_{T.M}$ is the strengthening effect caused by the thermal effect, k is a constant, G_m is the shear modulus of the solder matrix, b is the Burgers vector, $\Delta\alpha$ is the difference in CTE between the reinforcement and matrix, ΔT is the temperature difference between materials preparation and testing, V_r is the volume fraction of the reinforcement, and d_r is the size of reinforcement.

3.6. Long-term reliability of composite solder joints

To better evaluate the newly developed composite solder, soldering joint and their thermal aging test were conducted. In this part, the optimized composition, 0.05 wt% Ni-rGO reinforced Sn2.5Ag0.7Cu0.1Ce composite solder, was selected. In addition, the composition without Ni-rGO, Sn2.5Ag0.7Cu0.1Ce solder, was also selected as the reference.

Fig. 12(a) illustrates the evolution of shear strength for the composite solder joint during thermal aging. After reflow, the shear strength of the Sn2.5Ag0.7Cu0.1Ce solder joint is 33.5 MPa. After 500 h of thermal aging at 150 °C, the shear strength decreased to 27.1 MPa, representing a decrease of 19.1% compared to the after reflow. For the 0.05 wt% Ni-rGO reinforced Sn2.5Ag0.7Cu0.1Ce composite solder joint, the shear strength of the joint is 37.6 MPa after reflow, which is higher than that of the Sn2.5Ag0.7Cu0.1Ce solder joint. After 500 h of thermal aging, the shear strength of the composite solder joint decreased to 33.1 MPa, representing a decrease of 12.0% compared to the initial stage. While it still higher than that of the Sn2.5Ag0.7Cu0.1Ce solder joint after reflow. Furthermore, even after long-term thermal aging (500 h), the strength of the composite solder joint remains higher than that of the Sn2.5Ag0.7-Cu0.1Ce solder joint. This indicates that the newly developed composite solder exhibits good reliability.

Fig. 12(c) shows the SEM images of the Sn2.5Ag0.7Cu0.1Ce solder joint after reflow. As seen that the sold0er joint consists of three parts: the Cu substrate, interfacial IMC, and solder seam. The interfacial IMC, as an important part of the solder joint, is closely related to its reliability. According to the Gibbs free energy curve of the Cu–Sn binary system, when the ratio of Cu: Sn atoms is 6: 5, the system's free energy is minimized [55]. Therefore, during soldering, the liquid solder reacts with the Cu substrate to form Cu_6Sn_5 IMC, as previous studies have also confirmed [5]. In Fig. 12(a), the interfacial IMC Cu_6Sn_5 presents a scallop-like morphology, with an average thickness of 3.53 μm (shown in Fig. 12(b)). After 150 °C thermal aging for 500 h, the morphology and size of the interfacial IMC undergo significant changes (shown in Fig. 12 (c1)). The average thickness of the interfacial IMC of the Sn2.5Ag0.7-Cu0.1Ce solder joint increases to 9.51 μm (shown in Fig. 12(b)), which is 2.7 times that after reflow. Additionally, it can be observed in Fig. 12(c) that the interfacial IMC contains two parts: light-colored Cu_6Sn_5 and dark-colored Cu_3Sn near the substrate [17]. Furthermore, voids in the interface IMC layer are also observed. During thermal aging, the growth of interface IMC Cu_6Sn_5 mainly results from the diffusion of Sn atoms in the solder and Cu atoms in the substrate. As the thickness of the interface IMC Cu_6Sn_5 increases, the diffusion of Sn atoms towards the Cu substrate side is gradually hindered. When the supply of Sn atoms on the Cu substrate side is insufficient, interface Cu_6Sn_5 will react with Cu atoms in the substrate to form Cu_3Sn [56]. Due to the occurrence of this non-equilibrium diffusion, Kirkendall voids are eventually generated, as shown in Fig. 12(c1). Similar results have been reported in the literature [57]. These factors lead to a decrease in the shear strength of the solder joint. Fig. 12(d) shows the Ni-rGO reinforced Sn2.5Ag0.7Cu0.1Ce composite solder joint after reflow. The interfacial IMC Cu_6Sn_5 also presents a scallop-like morphology, with a corresponding interfacial IMC thickness of 2.91 μm, smaller than that in Fig. 12(c). This is because during soldering, the presence of Ni-rGO blocks some diffusion channels between Sn and Cu, thereby inhibiting the growth of the interface IMC. After 500 h of thermal aging (shown in Fig. 12(d1)), the thickness of the

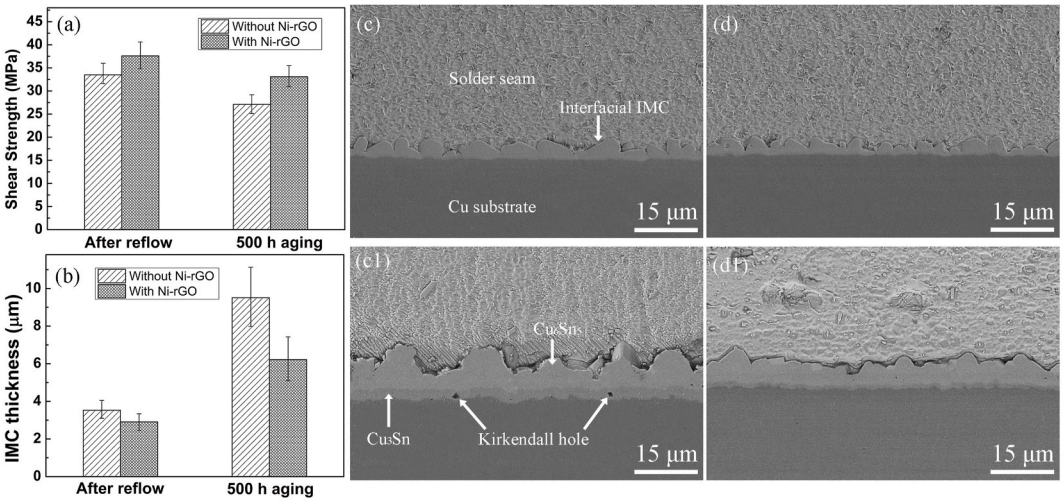

Fig. 12. Shear strength and interfacial IMC evolution of composite solder joint during thermal aging at 150 °C. (a) Shear strength, and (b) interfacial IMC thickness evolution during thermal aging. Sn2.5Ag0.7Cu0.1Ce solder joint after (c) reflow, and (c1) 500 h thermal aging at 150 °C. 0.05 wt% Ni-rGO reinforced Sn2.5Ag0.7Cu0.1Ce composite solder joint after (d) reflow, (d1) 500 h thermal aging at 150 °C.

interface IMC increases to 6.22 μm, which is 34.6% lower than that without Ni-rGO. Furthermore, compared to Fig. 12(c1), no Kirkendall voids are observed, indicating better microstructure reliability. This also explains why the shear strength of the composite solder joint remains higher than that of the Sn2.5Ag0.7Cu0.1Ce solder joint after long-term thermal aging.

Fig. 13(a) shows the fracture surface of the Sn2.5Ag0.7Cu0.1Ce solder joint after reflow. The fracture surface exhibits numerous dimples, characteristic of ductile fracture, with a microvoid coalescence fracture mechanism. The fracture occurs in the solder seam region. This is because after reflow, a well-metallurgically bonded interface is formed, and the thickness of the interface IMC is relatively thin, so the weak area of the solder joint is in the solder seam region, where the fracture occurs. After 500 h of thermal aging (Fig. 13(c)), the fracture surface of the Sn2.5Ag0.7Cu0.1Ce solder joint undergoes significant changes. the number of dimples is reduced, and both dimples and cleavage planes are observed. This indicates that part of the fracture occurs in the solder seam region, and part occurs in the interfacial IMC region. This result can be explained by Fig. 12(c1). After 500 h of thermal aging, coarsening of the interface IMC occurs in the Sn2.5Ag0.7Cu0.1Ce solder joint, along with the presence of Kirkendall voids, making the interface IMC region a weak area in terms of performance, leading to fracture in the interface IMC region. Fig. 13(b) shows the fracture surface of the 0.05 wt% Ni-rGO reinforced Sn2.5Ag0.7Cu0.1Ce composite solder joint after reflow. The fracture surface also exhibits numerous dimples, characteristic of ductile fracture, with a fracture mechanism of microvoid coalescence. Additionally, there are more dimples, attributed to the refined microstructure of the composite solder joint. After 500 h of thermal aging (Fig. 13(d)), the fracture surface of the composite solder joint still consists of dimples, indicating that the fracture still occurs in the solder seam region.

In summary, the 0.05 wt% Ni-rGO reinforced Sn2.5Ag0.7Cu0.1Ce composite solder joint exhibits better shear strength than that of the Sn2.5Ag0.7Cu0.1Ce solder joint after reflow and 500 h of thermal aging. This indicates that the 0.05 wt% Ni-rGO reinforced Sn2.5Ag0.7Cu0.1Ce composite solder joint has good long-term reliability.

4. Conclusions

1 Ni nanoparticles uniformly adhered to the surface of rGO with a size of 26.3 nm, Ni-rGO is successfully obtained using thermal decomposition method. The effective incorporation of Ni-rGO into the solder matrix was achieved using the firstly proposed powder-melting method, offering a new approach for the development of low-melting-point composite materials.

2 The microstructure of the composite solder consists of typical β-Sn and eutectic structures. With the addition of Ni-rGO, the grain size gradually decreases, and the eutectic structures increase. Deep etching results revealed that columnar β-Sn is stacked from layered β-Sn, while Ag_3Sn in the eutectic exhibits sheet-like and needle-like distributions. The addition of 0.05 wt% Ni-rGO leads to an increase in sheet-like Ag_3Sn within the eutectics. Ni-rGO was found at the grain boundaries of composite solder, serving as nucleation sites for Ag_3Sn and Cu_6Sn_5.

3 The appropriate addition of Ni-rGO effectively improves the wettability of the composite solder. When Ni-rGO is added up to 0.05 wt%, the spreading area increase by 36.5% compared to the non-additive composition. Additionally, the resistivity of the composite solder falls within the range of 12.0–12.9 μΩ cm, with Ce and Ni-rGO addition having little impact on the electrical resistance.

4 The UTS of the composite solder exhibits a trend of initially increasing and then decreasing with the addition of Ni-rGO. The fracture mechanism evolves from predominantly ductile fracture characterized by dimples to a ductile-brittle mixed fracture consisting of dimples and cleavage planes. At an addition of 0.05 wt%, the tensile strength reaches a maximum of 58.1 MPa, a 15.0% improvement compared to the non-additive state, also surpassing the strength of commercial Sn3.0Ag0.5Cu lead-free solders. Concurrently, the elongation of the composite solder reaches 33.8%, demonstrating the achievement of a high-strength and tough Ni-rGO reinforced Sn2.5Ag0.7Cu0.1Ce composite solder.

5 The 0.05 wt% Ni-rGO reinforced Sn2.5Ag0.7Cu0.1Ce composite solder joint exhibits better shear strength than that of the Sn2.5Ag0.7Cu0.1Ce solder joint after reflow and 500 h of thermal aging. This indicates that the 0.05 wt% Ni-rGO reinforced Sn2.5Ag0.7Cu0.1Ce composite solder joint has good long-term reliability.

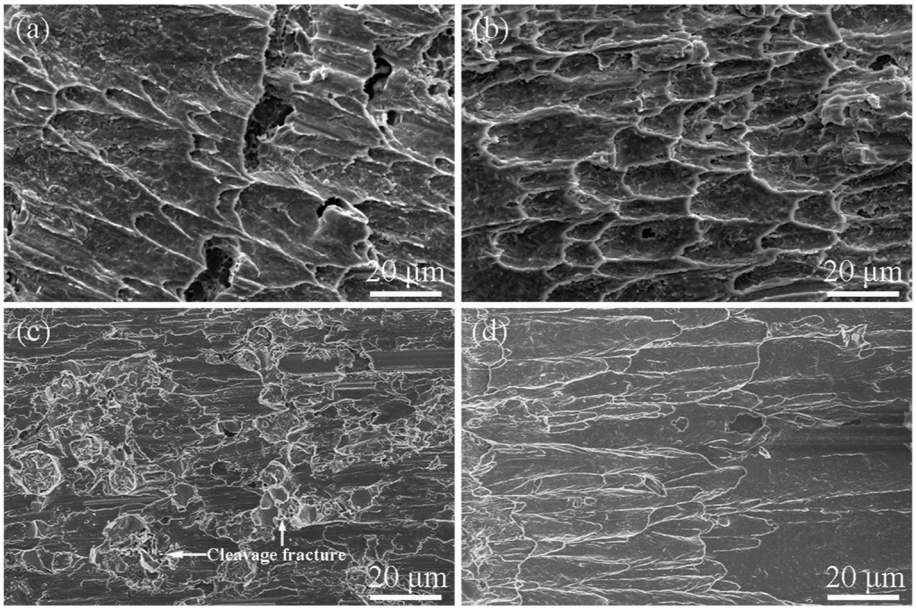

Fig. 13. Fracture surface evolution of composite solder joints during thermal aging at 150 °C. Sn2.5Ag0.7Cu0.1Ce solder joint after (a) reflow, and (c) 500 h thermal aging at 150 °C. 0.05 wt% Ni-rGO reinforced Sn2.5Ag0.7Cu0.1Ce composite solder joint after (b) reflow, (d) 500 h thermal aging at 150°C.

Declaration of competing interest

The authors declare that they have no known competing financial interests or personal relationships that could have appeared to influence the work reported in this paper.

Acknowledgements

This work was supported by a project (JPNP20004) commissioned by the New Energy and Industrial Technology Development Organization (NEDO) and JSPS KAKENHI Grant Number JP22K04243, and by a research grant from The Murata Science Foundation.

Appendix A. Supplementary data

Supplementary data to this article can be found online at https://doi.org/10.1016/j.jmrt.2024.07.071.

References

[1] Zhang P, Xue S, Wang J. New challenges of miniaturization of electronic devices: electromigration and thermomigration in lead-free solder joints. Mater Des 2020; 192:108726. https://doi.org/10.1016/j.matdes.2020.108726.
[2] Zhang S, Duan R, Xu S, Xue P, Wang C, Chen J, et al. Shear performance and accelerated reliability of solder interconnects for fan-out wafer-level package. J Adv Join Process 2022;5:100076. https://doi.org/10.1016/j.jajp.2021.100076.
[3] Zhang L, Liu Z quan, Chen SW, Wang Y dong, Long WM, Guo Y huan, et al. Materials, processing and reliability of low temperature bonding in 3D chip stacking. J Alloys Compd 2018;750:980–95. https://doi.org/10.1016/j.jallcom.2018.04.040.
[4] He H, Peng W, Liu J, Chan XY, Liu S, Lu L, et al. Microstructured BN composites with internally designed high thermal conductivity paths for 3D electronic packaging. Adv Mater 2022;2205120:1–11. https://doi.org/10.1002/adma.202205120.
[5] Xiong M yue, Zhang L. Interface reaction and intermetallic compound growth behavior of Sn-Ag-Cu lead-free solder joints on different substrates in electronic packaging. J Mater Sci 2019;54:1741–68. https://doi.org/10.1007/s10853-018-2907-y.
[6] Xiong C, Xiao Y, Zhang J, Luo D, Goodall R. Microstructure transformation and mechanical properties of Al alloy joints soldered with Ni-Cu foam/Sn-3.0Ag-0.5Cu (SAC305) composite solder. J Alloys Compd 2022;922:166135. https://doi.org/10.1016/j.jallcom.2022.166135.
[7] El-Daly AA, Ibrahiem AA, Abdo MA, Eid NAM. Viscoplastic characterization and mechanical strength of novel Sn–1.7Ag–0.7Cu lead-free solder alloys with microalloying of Te and Co. J Mater Sci Mater Electron 2019;30:12937–49. https://doi.org/10.1007/s10854-019-01656-8.
[8] Zhang L, Xue SB, Gao LL, Sheng Z, Zeng G, Chen Y, et al. Properties of SnAgCu/SnAgCuCe soldered joints for electronic packaging. J Mater Sci Mater Electron 2010;21:635–42. https://doi.org/10.1007/s10854-009-9969-1.
[9] Belyakov SA, Xian J, Zeng G, Sweatman K, Nishimura T, Akaiwa T, et al. Precipitation and coarsening of bismuth plates in Sn–Ag–Cu–Bi and Sn–Cu–Ni–Bi solder joints. J Mater Sci Mater Electron 2019;30:378–90. https://doi.org/10.1007/s10854-018-0302-8.
[10] Illés B, Choi H, Byun J, Dušek K, Bušek D, Skwarek A. Incorporation and corrosion protection mechanism of TiO_2 nano-particles in SnAgCu composite alloys: experimental and density functional theory study. Ceram Int 2023;49:23765–74. https://doi.org/10.1016/j.ceramint.2023.04.216.
[11] El-Daly AA, Fawzy A, Mansour SF, Younis MJ. Novel SiC nanoparticles-containing Sn-1.0Ag-0.5Cu solder with good drop impact performance. Mater Sci Eng 2013; 578:62–71. https://doi.org/10.1016/j.msea.2013.04.022.
[12] Wang H, Hu X, Jiang X. Effects of Ni modified MWCNTs on the microstructural evolution and shear strength of Sn-3.0Ag-0.5Cu composite solder joints. Mater Char 2020;163. https://doi.org/10.1016/j.matchar.2020.110287.
[13] Nazarewicz W, Riley MA, Garrett JD. Equilibrium deformations and excitation energies of single-quasiproton band heads of rare-earth nuclei. Nucl Physics, Sect A 1990;512:61–96. https://doi.org/10.1016/0375-9474(90)90004-6.
[14] Liu J, Kong X, Zheng L, Guo X, Liu X, Shui J. Rare earth single-atom catalysts for nitrogen and carbon dioxide reduction. ACS Nano 2020;14:1093–101. https://doi.org/10.1021/acsnano.9b08835.
[15] Wang H, Kang J, Wang Y. Discovery and identification of arsenic removal products from molten steel by adding rare earth. J Mater Res Technol 2022;18:2922–31. https://doi.org/10.1016/j.jmrt.2022.03.171.
[16] Zhang Z, Jiang W, guan F, Li G, Fan Z. Interface formation and strengthening mechanisms of Al/Mg bimetallic composite via compound casting with rare earth Ce introduction. Mater Sci Eng 2022;854:143830. https://doi.org/10.1016/j.msea.2022.143830.
[17] Zhang L, Xue SB, Zeng G, Gao LL, Ye H. Interface reaction between SnAgCu/SnAgCuCe solders and Cu substrate subjected to thermal cycling and isothermal aging. J Alloys Compd 2011;510:38–45. https://doi.org/10.1016/j.jallcom.2011.08.044.
[18] Wang Y, Zhao XC, Liu Y, Wang Y, Li DM. Microstructure, wetting property of Sn–Ag–Cu–Bi–xCe solder and IMC growth at solder/Cu interface during thermal cycling. Rare Met 2021;40:714–9. https://doi.org/10.1007/s12598-015-0526-1.
[19] Zhang H, Yang D, Lau A, Ma T, Lin H, Jia B. Hybridized graphene for supercapacitors: beyond the limitation of pure graphene. Small 2021;17:1–22. https://doi.org/10.1002/smll.202007311.
[20] Liu XD, Han YD, Jing HY, Wei J, Xu LY. Effect of graphene nanosheets reinforcement on the performance of SnAgCu lead-free solder. Mater Sci Eng 2013; 562:25–32. https://doi.org/10.1016/j.msea.2012.10.079.
[21] Han YD, Gao Y, Jing HY, Wei J, Zhao L, Xu LY. A modified constitutive model of Ag nanoparticle-modified graphene/Sn–Ag–Cu/Cu solder joints. Mater Sci Eng 2020; 777. https://doi.org/10.1016/j.msea.2020.139080.
[22] Herold F, Prosch S, Oefner N, Brunnengräber K, Leubner O, Hermans Y, et al. Nanoscale hybrid amorphous/graphitic carbon as key towards next-generation carbon-based oxidative dehydrogenation catalysts. Angew Chem Int Ed 2021;60: 5898–906. https://doi.org/10.1002/anie.202014862.
[23] Huo F, Zhang K, Zhang M, Wang H. Preparation by ball milling–thermal decomposition method and characterization of reduced graphene oxide decorated with Ni nanoparticles. Jom 2019;71:4264–73. https://doi.org/10.1007/s11837-019-03527-3.
[24] Chen Z, Cai M, Liu Z, Chen Y, Yi X, Wang F, et al. Amorphization and intermetallic nucleation in early-stage interfacial diffusion during Sn-solder/Ni solid-state bonding. J Alloys Compd 2021;859:158399. https://doi.org/10.1016/j.jallcom.2020.158399.
[25] Muench F, Schaefer S, Méndez M, Fernández-Roldán JA, González-García AS, Vega V, et al. Magneto-structural properties of rhombohedral Ni and Ni-B nanotubes deposited by electroless-plating in track-etched mica templates. J Mater Chem C 2023;11:9271–80. https://doi.org/10.1039/d3tc00857f.
[26] Gupta B, Kumar N, Panda K, Kanan V, Joshi S, Visoly-Fisher I. Role of oxygen functional groups in reduced graphene oxide for lubrication. Sci Rep 2017;7:1–14. https://doi.org/10.1038/srep45030.
[27] Chen WX, Xue SB, Wang H. Wetting properties and interfacial microstructures of Sn-Zn-xGa solders on Cu substrate. Mater Des 2010;31:2196–200. https://doi.org/10.1016/j.matdes.2009.10.053.
[28] Li X, Minor AM. Precise measurement of activation parameters for individual dislocation nucleation during in situ TEM tensile testing of single crystal nickel. Scripta Mater 2021;197:113764. https://doi.org/10.1016/j.scriptamat.2021.113764.
[29] Bharath Krupa Teja M, Sharma A, Das S, Das K. A review on nanodispersed lead-free solders in electronics: synthesis, microstructure and intermetallic growth characteristics. J Mater Sci 2022;57:8597–633. https://doi.org/10.1007/s10853-022-07187-8.
[30] Kanchan BK, Randive P. Investigation on capacity extension through non-uniform anode microstructure in lithium-ion battery. Int J Heat Mass Tran 2023;214: 124413. https://doi.org/10.1016/j.ijheatmasstransfer.2023.124413.
[31] Huo F, Jin Z, Le Han D, Zhang K, Nishikawa H. Interface design and the strengthening-ductility behavior of tetra-needle-like ZnO whisker reinforced Sn1.0Ag0.5Cu composite solders prepared with ultrasonic agitation. Mater Des 2021;210:110038. https://doi.org/10.1016/j.matdes.2021.110038.
[32] Gain AK, Zhang L. Microstructure, mechanical and electrical performances of zirconia nanoparticles-doped tin-silver-copper solder alloys. J Mater Sci Mater Electron 2016;27:7524–33. https://doi.org/10.1007/s10854-016-4732-x.
[33] Tu X, Yi D, Wu J, Wang B. Influence of Ce addition on Sn-3.0Ag-0.5Cu solder joints: thermal behavior, microstructure and mechanical properties. J Alloys Compd 2017;698:317–28. https://doi.org/10.1016/j.jallcom.2016.12.191.
[34] Drienovsky M, Trnkova LR, Martinkovic M, Ozvold M, Cernickova I, Palcut M, et al. Influence of cerium addition on microstructure and properties of Sn-Cu-(Ag) solder alloys. Mater Sci Eng 2015;623:83–91. https://doi.org/10.1016/j.msea.2014.11.033.
[35] Cantwell PR, Tang M, Dillon SJ, Luo J, Rohrer GS, Harmer MP. Grain boundary complexions. Acta Mater 2014;62:1–48. https://doi.org/10.1016/j.actamat.2013.07.037.
[36] Nam S, Chang K, Lee W, Kim MJ, Hwang JY, Choi H. Structural effect of two-dimensional BNNS on grain growth suppressing behaviors in Al-matrix nanocomposites. Sci Rep 2018;8:1–12. https://doi.org/10.1038/s41598-018-20150-5.
[37] Zeng G, Callaghan MD, McDonald SD, Yasuda H, Nogita K. In situ studies revealing dendrite and eutectic growth during the solidification of Sn-0.7Cu-0.5Ag Pb-free solder alloy. J Alloys Compd 2019;797:804–10. https://doi.org/10.1016/j.jallcom.2019.04.153.
[38] Tan CY, Salleh MAAM, Saud N, Chaiprapa J, Nogita K. Grain refinement of primary Cu6Sn5 in the Sn-3wt%Ag-5wt%Cu alloy by Ge. J Mater Res Technol 2022;21: 3301–12. https://doi.org/10.1016/j.jmrt.2022.10.128.
[39] Cui Y, Xian JW, Zois A, Marquardt K, Yasuda H, Gourlay CM. Nucleation and growth of Ag3Sn in Sn-Ag and Sn-Ag-Cu solder alloys. Acta Mater 2023;249. https://doi.org/10.1016/j.actamat.2023.118831.
[40] Zadymova NM, Dolzhikova VD, Kharlov AE. Adsorption of a lipophilic drug, felodipine, at different interfaces. Colloid J 2020;82:376–83. https://doi.org/10.1134/S1061933X20030151.
[41] Jung DH, Sharma A, Jung JP. Influence of dual ceramic nanomaterials on the solderability and interfacial reactions between lead-free Sn-Ag-Cu and a Cu conductor. J Alloys Compd 2018;743:300–13. https://doi.org/10.1016/j.jallcom.2018.02.017.
[42] Ismail N, Jalar A, Afdzaluddin A, Bakar MA. Electrical resistivity of Sn–3.0Ag–0.5Cu solder joint with the incorporation of carbon nanotubes.

Nanomater Nanotechnol 2021;11:1–9. https://doi.org/10.1177/1847980421996539.
[43] Amin NAAM, Shnawah DA, Said SM, Sabri MFM, Arof H. Effect of Ag content and the minor alloying element Fe on the electrical resistivity of Sn-Ag-Cu solder alloy. J Alloys Compd 2014;599:114–20. https://doi.org/10.1016/j.jallcom.2014.02.100.
[44] Kim KW, Pashkin A, Schäfer H, Beyer M, Porer M, Wolf T, et al. Ultrafast transient generation of spin-density-wave order in the normal state of $BaFe_2As_2$ driven by coherent lattice vibrations. Nat Mater 2012;11:497–501. https://doi.org/10.1038/nmat3294.
[45] Ren Q, Fu C, Qiu Q, Dai S, Liu Z, Masuda T, et al. Establishing the carrier scattering phase diagram for ZrNiSn-based half-Heusler thermoelectric materials. Nat Commun 2020;11:1–9. https://doi.org/10.1038/s41467-020-16913-2.
[46] Pan S, Wang T, Jin K, Cai X. Understanding and designing metal matrix nanocomposites with high electrical conductivity: a review. J Mater Sci 2022;57:6487–523. https://doi.org/10.1007/s10853-022-07010-4.
[47] El-Daly AA, Desoky WM, Elmosalami TA, El-Shaarawy MG, Abdraboh AM. Microstructural modifications and properties of SiC nanoparticles-reinforced Sn-3.0Ag-0.5Cu solder alloy. Mater Des 2015;65:1196–204. https://doi.org/10.1016/j.matdes.2014.08.058.
[48] Vafaeenezhad H, Aliakbari-Sani S, Seyedein SH, Aboutalebi MR, Eivani AR. Dislocation density and twinning-related constitutive modeling of substructural evolution in Sn-5Sb-0.5(Ag/Cu) alloys under monotonic deformation. J Alloys Compd 2023;938:168516. https://doi.org/10.1016/j.jallcom.2022.168516.
[49] Li Y, Ding Y, Li C en, Ren J, Ran G. Dislocations generated by pre-strain dominate the subsequent plastic deformation. Mater Sci Eng 2023;887:145716. https://doi.org/10.1016/j.msea.2023.145716.
[50] Peng Z, Wang X, Wu Z. A bundle-based shear-lag model for tensile failure prediction of unidirectional fiber-reinforced polymer composites. Mater Des 2020;196:109103. https://doi.org/10.1016/j.matdes.2020.109103.
[51] Cox HL. The elasticity and strength of paper and other fibrous materials. Br J Appl Phys 1952;3:72–9. https://doi.org/10.1088/0508-3443/3/3/302.
[52] Hu ZY, Cheng XW, Li SL, Zhang HM, Wang H, Zhang ZH, et al. Investigation on the microstructure, room and high temperature mechanical behaviors and strengthening mechanisms of the (TiB+TiC)/TC4 composites. J Alloys Compd 2017;726:240–53. https://doi.org/10.1016/j.jallcom.2017.08.017.
[53] Shi W, Yan Q, Shen J, Chen B, Li Y. Quasi-continuous GNS network induced local dynamic recrystallization along interfaces in titanium MMCs under high strain rate loading. Mater Sci Eng 2022;852:143723. https://doi.org/10.1016/j.msea.2022.143723.
[54] Bembalge OB, Panigrahi SK. Development and strengthening mechanisms of bulk ultrafine grained AA6063/SiC composite sheets with varying reinforcement size ranging from nano to micro domain. J Alloys Compd 2018;766:355–72. https://doi.org/10.1016/j.jallcom.2018.06.306.
[55] Ke JH, Gao Y, Kao CR, Wang Y. Pattern formation during interfacial reaction in-between liquid Sn and Cu substrates - a simulation study. Acta Mater 2016;113:245–58. https://doi.org/10.1016/j.actamat.2016.05.004.
[56] Zhang Z, Cao H, Li M, Yu Y, Yang H, Yang S. Three-dimensional placement rules of Cu6Sn5 textures formed on the (111)Cu and (001)Cu surfaces using electron backscattered diffraction. Mater Des 2016;94:280–5. https://doi.org/10.1016/j.matdes.2016.01.037.
[57] Wang J, Chen J, Zhang L, Zhang Z, Han Y, Hu X, et al. Forming mechanism and growth of Kirkendall voids of Sn/Cu joints for electronic packaging: a recent review. J Adv Join Process 2022;6:100125. https://doi.org/10.1016/j.jajp.2022.100125.